Bull Eng Geol Environ (2019) 78:763–777
DOI 10.1007/s10064-017-1129-x

ORIGINAL PAPER

Dynamic process simulation of construction solid waste (CSW) landfill landslide based on SPH considering dilatancy effects

Heng Liang[1,2] · Siming He[1,3,4] · Xiaoqin Lei[1,3] · Yuzhang Bi[5] · Wei Liu[1,2] · Chaojun Ouyang[1,3]

Received: 12 February 2017 / Accepted: 11 July 2017 / Published online: 17 July 2017

Abstract Construction solid waste (CSW) landfill landslides, such as the Guangming New District landslide, which occurred in Shenzhen (hereafter the Shenzhen landslide), occur when the material is loose and saturated. They usually exhibit characteristics such as abrupt failure and whole collapse. During the propagation of landslides, dilatation behavior plays an important role in causing liquefaction, resulting in high velocity and exceptionally long run-out dynamics. We propose a dynamic model for describing fluidized CSW landslides by integrating the dilatancy model into smoothed particle hydrodynamics (SPH). The dilatancy model implies that the occurrence of dilation or the contraction of the granular-fluid mixture depends on the initial solid volume fraction. The dynamic model is used to simulate the Shenzhen landslide, and special attention is paid to the effects of different initial solid volumes on the mobility of the CSW landslide. The results show that when the solid volume fraction is higher than the critical value, contraction occurs, the excess pore water pressure increases, and the basal friction resistance is reduced. CSW landslide mobility is based on the initial solid volume fraction (or initial void ratio) of the granular-fluid mixture; a slight change in the initial volume fraction significantly affects the mobility of the CSW landfill landslide.

Keywords CSW landfill landslide · Dilatancy effects · Dynamic processes · SPH

List of symbols

b	Proportionality coefficient
c	Cohesion
$\dot{e}_{ij}$	Deviatoric strain-rate tensor
G	Shear modulus of soil skeleton
K_1	Bulk modulus of soil skeleton
K_m	Bulk modulus of solid particles
K_s	Bulk modulus of solid particles
K_w	Bulk modulus of water
K_t	Total bulk modulus
L_M	Maximum source area material migration displacement
m_0	Initial solid volume fraction
m_s	Current solid volume fraction
m_w	Current water volume fraction
m_a	Current air volume fraction
m_{eq}	Equilibrium solid volume fraction
m_{crit}	Lithostatic critical-state solid volume fraction
N	Generalized dimensionless parameter
p_0^a	Standard atmospheric pressure
Δp^a	Pressure increment
s_{ij}^N	New second invariant of deviatoric stress tensor
u_w	Pore water pressure
u_a	Pore air pressure
u_s	Matric suction
u_f	Pore fluid pressure
Δu_f^e	Excess pore fluid pressure increment
u_t^C	Corrected values of pore fluid pressure

✉ Siming He
726483842@qq.com

[1] Institute of Mountain Hazards and Environment, Chinese Academy of Sciences, Chengdu, China

[2] University of Chinese Academy of Sciences, Beijing, China

[3] Key Laboratory of Mountain Hazards and Surface Process, Chinese Academy of Sciences, Chengdu, China

[4] CAS Center for Excellence in Tibetan Plateau Earth Sciences, Chengdu, China

[5] Southeast University, Nanjing, China

u_f^N	New pore fluid pressure
v_0	Total volume
$\dot{\gamma}$	Shear strain-rate
$\Delta\gamma$	Shear strain increment
δ_{ij}	Kronecker's delta
μ	Effective shear viscosity of pore fluid
ρ	Current mixture bulk density
ρ_0	Initial mixture bulk density
ρ_s	Soil grain density
ρ_w	Initial fluid phase density
ε_v	Volume strain of solid skeleton
$\Delta\varepsilon_v^e$	Volume strain increment
ξ	Calibration constant
ζ	Characteristic grain diameter
σ_0	Reference mean stress
σ_e	Mean effective stress
σ_t	Mean total stress
σ_t^C	Corrected values of total mean stress
σ_e^N	New effective stress
σ'_{ij}	Net stress tensor acting on solid skeleton
σ_{ij}^N	New total stress
σ_t^N	New total mean stress
τ_{min}	Minimum shear strength
τ_s	Shear stress
τ^N	New second deviatoric shear stress
ϕ	Internal friction angle
ψ	Dilatancy angle

Introduction

Rapid urban and infrastructure development has led to an increasing number of construction solid waste (CSW) landfills being established, and correspondingly, the number of CSW landfill landslides occurring around the world has increased (Colomer-Mendoza et al. 2013; Huang et al. 2013; Ouyang et al. 2016; Yin et al. 2016). On December 20, 2015, a CSW landfill landslide occurred in Shenzhen, Guangdong, China, causing 77 deaths and destroying 33 houses. The most obvious feature of the landslide was that its traveling distance exceeded 1.2 km and the landslide mobility index ($H_M/L_M = 0.092$) was much lower than that of a general landslide (Ouyang et al. 2016; Yin et al. 2016). A landslide mobility index lower than 0.3 denotes high mobility. However, not much is known about the complex CSW landfill material transport mechanism during landslide propagation. Some extensive transport mechanisms have been proposed to explain the hypermobility of catastrophic landslides' dynamic processes, including the evaluation of pore fluid pressure (Iverson et al. 2000; Ouyang et al. 2016), entrainment (McDougall and Hungr 2005), dynamic fragmentation (Davies and McSaveney 2009), velocity weakening (Lucas et al. 2014), and fluidization (Ochiai et al. 2004). The CSW landfill is a loose and saturated grain-water mixture. The interaction between the fluid and solid phases of the mixture depends on the pore water pressure, which determines the effective stress and friction resistance applied to the grain medium in dynamic processes (Iverson 2000, 2005). Thus, pore water pressure plays a key role in dynamic processes. A slight deformation can induce the contraction of a loose grain fluid mixture, which may lead to the generation of excess pore water pressure. Depending on whether the solid volume fraction is higher or lower than the critical value, the slight deformation may also lead to dilation or contraction of the fluid-granular mixture material (Bouchut et al. 2016; George and Iverson 2014).

Pore fluid pressure is related to the dilation and contraction behaviors, when subject to shear deformation (Bouchut et al. 2016). The dilation of the solid phase can induce the absorption of fluid into the mixture, which decreases the pore fluid pressure and, therefore, increases the effective stress. On the other hand, the contraction of the solid phase can induce the extrusion of fluid, which increases the pore fluid pressure and decreases the effective stress. The initial solid volume fraction can highly influence the dilation and contraction of the mixture (Ouyang et al. 2016; Wang and Sassa 2003). The shear deformation controls the dilation behavior of dense granular materials and the contraction behavior of loose granular materials. Taking into account the dilatancy effects in the dynamic evolution processes of fluid-granular mixtures, different dilatancy models have been proposed based on the depth-averaged continuum description. Unlike the traditional rheology models (Chen 1987; Huang et al. 2011, 2012; Iverson 2003; Pastor et al. 2009a, b), dilatancy models are generally based on Jackson's (2000) model, which describes the interaction between the fluid and solid phases. The key role of these dilatancy models is the combination of the dilation and contraction behaviors with the equilibrium solid volume fraction, which is related to the solid volume fraction and effective stress (Bouchut et al. 2016; Iverson and George 2016; Gray and Edwards 2014; Iverson and George 2014, 2016; Pastor et al. 2009a, b; Sheng et al. 2013). Focusing on this aspect, the dilation rate is described by $\dot{\gamma}\tan\psi$ (Bouchut et al. 2016; Iverson and George 2016; Iverson and George 2014, 2016), where $\dot{\gamma}$ is the shear strain rate and ψ is the dilatancy angle. The drag force is evaluated using the two-phase two-layer model proposed by (Bouchut et al. 2016). In contrast, Iverson's dilatancy model is a single-phase mixture model that ignores the drag force (Iverson and George 2014). In their models, the excess pore pressure is evaluated by a diffusion equation.

Grid- or mesh-based methods have been widely applied in various areas of computational fluid dynamics and

computational solid mechanics (Anderson and Wendt 1995; Fung and Tong 2001). However, the existence of the grid or mesh can cause various difficulties in solving problems related to the free surface, extremely large deformations, a deformable boundary, and a moving interface (Liu and Liu 2010). Mesh-free methods have been developed in the recent past (Liu and Gu 2005), and smoothed particle hydrodynamics (SPH) methods, which were invented to solve astrophysical problems, have been widely applied in many fields (Liu and Liu 2003; Lucy 1977; Violeau 2012). In recent years, the SPH method has been widely applied to simulate the movement processes of landslides, lahars, and liquefied soils (Cascini et al. 2012, 2014; Cola et al. 2008; Haddad et al. 2010; Huang and Dai 2014; Huang et al. 2012; Pastor et al. 2009a, b, 2014). Compared with Eulerian grid methods, free surfaces, material interfaces, and moving boundaries can be traced naturally by the SPH method (Liu and Liu 2010). Compared with the Lagrangian grid methods, the SPH method can avoid mesh distortion as well as the tedious and time-consuming re-mesh procedure (Liu and Liu 2003, 2010).

The aim of this study is to establish a constitutive model including the dilatancy effects based on the SPH method. The evaluation of the dilatancy angle is based on Iverson's model (Iverson and George 2014, 2016). The key point in our model is that the solid grain, water, and solid skeleton are compressible. The constitutive model is a single-phase mixture model without the drag force, and is suitable for the low permeability granular masses, such that the consolidation can be ignored during the short dynamic evolution process of a landslide. The model is applied to study the dynamic evolution process of the Shenzhen landfill landslide and the influence of the initial solid volume fraction on the CSW landfill motion.

Background of the Shenzhen landslide and SPH method

Geological conditions and soil properties

The Shenzhen landslide occurred at Guangming New District, Shenzhen, Guangdong, China. The location was a stone pit filled with about 90,000 m^3 water. The pit is surrounded by mountains on all sides except the north. The bedrock is 17 m higher than the pit bottom on the north side. The terrain slopes downward from the bedrock to the north, and the maximum value of slope angle in this area is about 22°. Loose CSW was dumped in the pit without excluding the bottom water, and an effective drainage system was not established. The landfill is ten storeys high, with an average gradient is 40%. The maximum elevation is about 160 m at the south edge and the minimum elevation is about 46 m at the north edge (at the bottom). The total volume of the landfill is about 5.83×10^4 m^3. The deposit area of this landslide has a south-north length of 726 m and an east–west width ranging between 150 and 630 m (Yin et al. 2016). The images and topographical contour maps of the source area and deposit area are demonstrated in Fig. 1 (from Yin et al. 2016).

The bedrock of the landfill is granite, and the soil properties in the source area and deposit area were tested in detail (Ouyang et al. 2016; Yin et al. 2016). According to Yin et al. (2016), the average density of the soil grains is 2650 kg/m^3, the average solid volume fraction is 0.51, saturation is 0.78, the internal friction angle is between 3.5° and 27°, the average cohesion is 11.87 kPa, the average modulus of compressibility is 3.5 MPa, and the maximum value of hydraulic conductivity in the deposit area is less than 1.0×10^{-7} m/s. According to Ouyang et al. (2016), the internal friction angle is 31.9°, the solid volume fraction of the dry soil is between 0.43 and 0.55, the saturation of the soil is unknown, and the cohesion is 4.7 kPa. The initial solid volume fraction is an important factor, as it affects the dilation or contraction behavior. According to Yin et al. (2016), the landfill was saturated before the landslide, and there was no water run off before and after the landslide because the consolidation was ignored. The initial solid volume fraction was 0.57 according to Yin et al. (2016).

The failure mechanism

As the drainage system was ineffective and the flood intercepting trench was not established to intercept the surface water on the slope, the CSW was saturated. The CSW was not compacted after being dumped. These conditions indicate that the landfill was loose and saturated. The soil in the sliding surface was liquefied (Ouyang et al. 2016), and the bottom of the deposited body exerted excess pore water pressure.

The initial solid volume fractions can affect the flow process of a landslide. The excess pore water pressure is related to the dilation and contraction behavior of soils, which is controlled by the effective stress, solid volume fraction, and shear strain rate (Bouchut et al. 2016; Iverson and George 2014, 2016). There was persistent creep deformation before the collapse of this landfill. This would have caused the contraction of the loose CSW and an increase in excess pore water pressure. With the increase in deformation, the pore pressure also increased and effective stress decreased. Thus, the solid–fluid mixture failed, and the landfill collapsed.

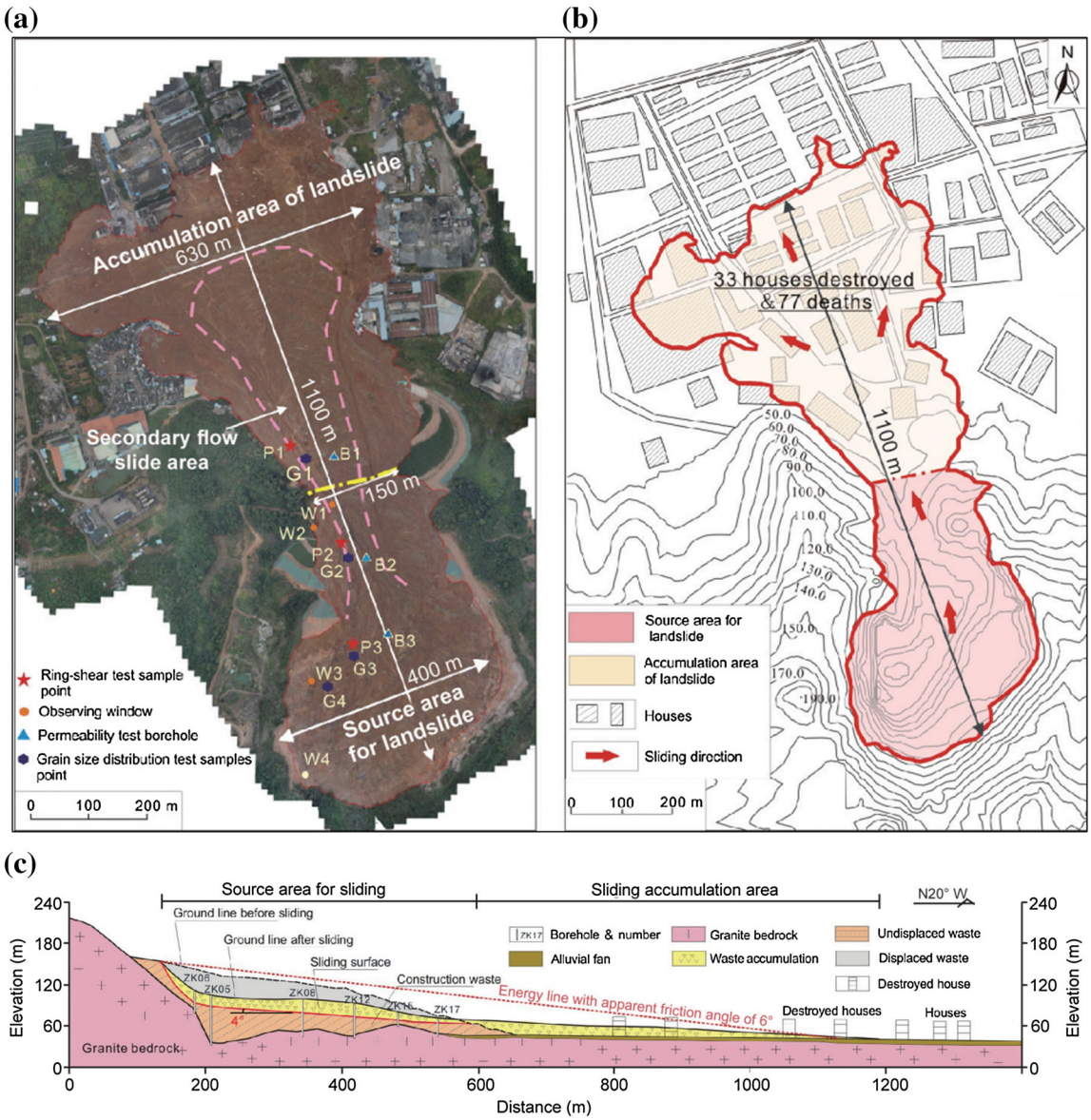

Fig. 1 Image, topographical contour map and cross-section view of the source area and deposit area (from Yin et al. 2016). **a** Image of the source area and deposit area. **b** Topographical contour map of the source area and deposit area. **c** Cross-section view of the Shenzhen landslide

The topography model

The topographical contour map can be used to determine the terrain before filling and before the landfill landslide occurred. Thus, the area and volume of the landfill body can be extracted. The terrain of the landfill before filling is shown in Fig. 2. Compared with the topographical contour map shown in Fig. 1, the buildings are ignored in the terrain model.

The landfill body is simulated by 53,271 smooth particles. The distance between the particles is 5 m, and the mass value of the particles can be calculated using the initial density and distance. The model of the landfill

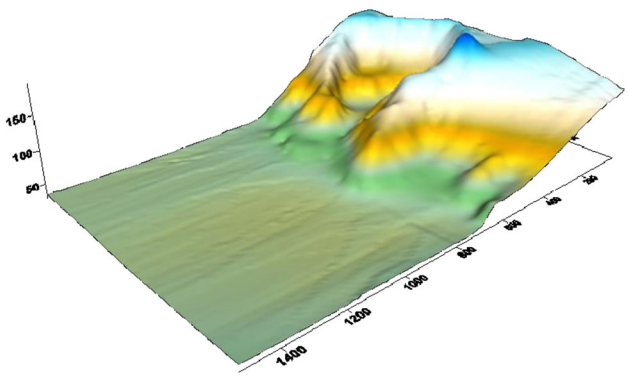

Fig. 2 Terrain image of the landfill before filling

before filling consists of 14,490 hexahedral grids. Given the existence of gravity, stress initialization is essential before the dynamic analysis is conducted; otherwise, an initial velocity will exist and affect the simulation results. The landfill model before the landslide is shown in Fig. 3, and the stress has been initialized before the dynamic simulation.

The SPH method

The SPH method is a mesh-free particle method. There are two steps in establishing SPH equations. The first step is integral approximations, and they are usually termed as kernel approximations. In the first step, the kernel approximation is based on the equation

$$f(\mathbf{x}) = \int_{\Omega} f(\mathbf{x}')\delta(\mathbf{x}-\mathbf{x}')\mathrm{d}\mathbf{x}', \tag{1}$$

where f is a function of the vector $\mathbf{x}$, and $\delta(\mathbf{x}-\mathbf{x}')$ is the Dirac delta function that is defined as

$$\delta(\mathbf{x}-\mathbf{x}') = \begin{cases} 1, & \mathbf{x}=\mathbf{x}' \\ 0, & \mathbf{x}\neq\mathbf{x}', \end{cases} \tag{2}$$

In Eq. (1), Ω is the integral volume that contains $\mathbf{x}$. In the first step, $\delta(\mathbf{x}-\mathbf{x}')$ can be replaced by a smoothing function $W(\mathbf{x}-\mathbf{x}',h)$ to approximate the equation, and the equation becomes

$$f(\mathbf{x}) \approx \int_{\Omega} f(\mathbf{x}')W(\mathbf{x}-\mathbf{x}',h)\mathrm{d}\mathbf{x}', \tag{3}$$

where h is the smoothing length to define the influence or support area of the smoothing function $W(\mathbf{x}-\mathbf{x}',h)$. In SPH, it can be written as

$$\langle f(\mathbf{x})\rangle = \int_{\Omega} f(\mathbf{x}')W(\mathbf{x}-\mathbf{x}',h)\mathrm{d}\mathbf{x}'. \tag{4}$$

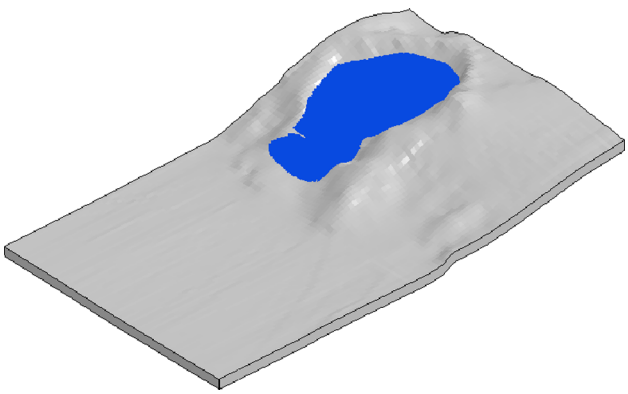

Fig. 3 The terrain image of the landfill after filling

The derivative of f can be written as

$$\langle \nabla\cdot f(\mathbf{x})\rangle = -\int_{\Omega} f(\mathbf{x}')\cdot\nabla W(\mathbf{x}-\mathbf{x}',h)\mathrm{d}\mathbf{x}'. \tag{5}$$

The smoothing function $W(\mathbf{x}-\mathbf{x}',h)$ should satisfy three conditions. The first condition is the normalization condition:

$$\int_{\Omega} W(\mathbf{x}-\mathbf{x}',h)\mathrm{d}\mathbf{x}' = 1. \tag{6}$$

The second condition is that the function should satisfy the Delta function property when h approaches zero:

$$\lim_{h\to 0} W(\mathbf{x}-\mathbf{x}',h) = \delta(\mathbf{x}-\mathbf{x}'). \tag{7}$$

The third condition is the compact condition:

$$W(\mathbf{x}-\mathbf{x}',h) = 0, \quad \text{when } |\mathbf{x}-\mathbf{x}'| > \kappa h, \tag{8}$$

where κ is a constant related to the smooth function for the particle at $\mathbf{x}$, and κh defines the effective area of the smooth function.

The second step is particle approximation; the discretization form of Eqs. (4) and (5) in the SPH method can be written as

$$\langle f(\mathbf{x})\rangle = \sum_{j=1}^{N} \frac{m_j}{\rho_j} f(\mathbf{x}_j)W(\mathbf{x}-\mathbf{x}_j,h), \tag{9}$$

$$\langle \nabla\cdot f(\mathbf{x})\rangle = -\sum_{j=1}^{N} \frac{m_j}{\rho_j} f(\mathbf{x}_j)\cdot\nabla W(\mathbf{x}-\mathbf{x}_j,h). \tag{10}$$

The continuous integral representation of function f and its derivatives can be converted into discrete summations of a set of particles by the particle approximation Eqs. (9) and (10). Particle summation to approximation is a key step that negates the necessity of the background mesh for the numerical integration in the SPH method.

Dilatancy model

The key reasons to establish the dilatancy model are to evaluate the dilatancy angle and pore fluid pressure. The dilation or contraction behavior is related to the solid volume fraction, shear strain rate, and effective stress. Our investigation into the Shenzhen landslide makes six simplified assumptions to calculate the relevant conditions, such as compressibility of the soil and dilatancy angle. Then, the shear stress, effective stress, and pore fluid pressure are calculated, and these conditions are then updated based on the stress–strain state.

Assumptions

Different states of air exist in soil, depending on the state of air bubbles inside water and the state of air–water separation (Hutter et al. 1999). The effective stress cannot increase until the water escapes, and the grains are rearranged and compacted (Major 2000). Thus, the effective stress increment during a flow process occurring within a short time can be ignored for low permeable soil. As a result, we ignore consolidation in our model. In the process of soil flow, the dilation and contraction behavior of the soil will increase or decrease the porosity rate depending on the increase and decrease, respectively, in the total volume v_0. Because water permeation is ignored during the flow process, we assume that the decrease in the porosity rate will lead to fluid compression, any increase in porosity will cause air entrainment, and the air–water mixture fluid comprises air bubbles inside the water during the flow process. The pore fluid pressure will cause compression of the mixture fluid and soil grains (Pastor et al. 2009a, b). Our model makes six assumptions:

(a) The consolidation can be ignored.
(b) The increase in v_0 will cause air entrainment.
(c) The fluid phase comprises the air–water mixture and air is insoluble.
(d) The fluid phase and soil grains are compressible.
(e) The flow process is homoiothermal.
(f) The matric suction can be ignored.

Density and volume fraction

Soil consists of a soil skeleton and a fluid phase. At the initial condition, the soil is saturated. The density of the soil grains is ρ_s, the initial solid volume fraction is m_0, the initial fluid phase volume fraction is $1 - m_0$, the initial fluid phase density is ρ_w, and the bulk density of the initial mixture ρ_0 is defined by

$$\rho_0 = \rho_s m_0 + \rho_w(1 - m_0). \tag{11}$$

In the flow process, the volume fraction of the soil skeleton will change, and air will enter the hole when the soil skeleton dilates. Then, the current mixture bulk density ρ is defined by

$$\rho = \rho_0/(1 + \varepsilon_v). \tag{12}$$

Because the volume modulus of the soil grains is much larger than the volume modulus of the soil skeleton and fluid phase, the deformation of the solid particles can be considered as negligible, and the current solid volume fraction m_s, the current water volume fraction m_w, and the current air volume fraction m_a, respectively, can be calculated by

$$m_s = m_0/(1 + \varepsilon_v), \tag{13}$$

$$m_w = (1-m_0)/(1 + \varepsilon_v), \tag{14}$$

$$m_a = \max(0,\ 1 - m_s - m_w), \tag{15}$$

where ε_v is the volumetric strain of the solid skeleton, which is equal to the volumetric strain of the fluidized soil.

Total stress, effective stress, and pore fluid pressure

For saturated soils, the fluid phase is water, and the mean effective stress σ_e can be calculated by

$$\sigma_e = \sigma_t - u_w, \tag{16}$$

where σ_t is the mean total stress, and u_w is the pore water pressure.

For unsaturated soil, the existence of matric suction causes the difference between the pore-air pressure and pore-water pressure (Sheng et al. 2008). Therefore,

$$\sigma'_{ij} = \sigma_{ij} - u_a\delta_{ij}, \tag{17}$$

$$u_s = u_a - u_w, \tag{18}$$

where σ'_{ij} is the net stress tensor acting on the solid skeleton, σ_{ij} is the total stress tensor acting on the fluid soil, u_a is the pore air pressure, δ_{ij} is Kronecker's delta, and u_s is the matric suction. In the previous assumption, the matric suction is ignored, and thus, $u_w = u_a = u_f$ and $\sigma_e = \sigma_t - u_f$, where u_f is the pore fluid pressure.

Compressibility of the fluidized soil

The total stress acting on soil mass can be divided into effective stress and pore fluid pressure. The effective stress results in volume deformation of the soil skeleton because of the change in the relative location of the soil particles and the pore fluid pressure result in the volume deformation of the pore fluid and solid particles. Because the pore fluid fills the soil skeleton, the volume deformation of the pore is equal to the volume deformation of the soil skeleton, and it is also equal to the volume deformation of the soil mass. In the above section, we assume that the fluid phase and soil particles are compressible, the compress process is homoiothermal, and the consolidation can be ignored. Thus, the volume deformation of the pore fluid and soil particles is equal to the volume deformation of the soil mass. A series of triaxial tests under low confining stress showed that the compression index of the soil is related to the solid volume fraction and mean effective stress (Major et al. 1997). The stress–strain relationships showed that the stresses achieved a plateau and further straining causes little stress change. An empirical formula was applied to evaluate the compressibility (Iverson and George 2014):

$$K_1 = -\frac{m_s(\sigma_e + \sigma_0)}{b}, \tag{19}$$

where K_1 is the bulk modulus of the soil skeleton, b is a proportionality coefficient, and σ_0 is the reference mean stress to limit the maximum compressibility. In our model, the bulk modulus of air is K_a, and the flow process is homoiothermal. Thus,

$$p_0^a = \left(1 + \frac{\Delta p^a}{K_a}\right)(p_0^a + \Delta p^a), \tag{20}$$

where p_0^a is the standard atmospheric pressure, and Δp^a is the pressure increment. Then,

$$K_a = -p_0^a - \Delta p^a. \tag{21}$$

The deformation caused by the pore fluid pressure can be decomposed into the deformation of the solid particles, water, and air. Because the matric suction is ignored and air is insoluble, the pore-water pressure is equal to the pore-air pressure. The bulk modulus of the mixture is

$$\frac{1}{K_m} = \frac{m_s}{K_s} + \frac{m_w}{K_w} + \frac{m_a}{K_a}, \tag{22}$$

where K_m is the bulk modulus of the solid particles, water, and air mixture; K_s is the bulk modulus of the solid particles, and K_w is the bulk modulus of water. K_s is difficult to test, and the function of K_s is to limit the maximum value of K_m. We have previously introduced the bulk modulus of the solid skeleton and the mixed bulk modulus of the solid particles, water, and air. The total bulk modulus K_t can be calculated by

$$K_t = K_1 + K_m. \tag{23}$$

Dilatancy angle

The total friction angle is not specified during the flow process (Iverson and George 2016). The dilatancy angle is related to the strain rate, effective stress, and voids ratio (Bolton 1984; Iverson and George 2014, 2016; Pailha and Pouliquen 2009). For dry granular material, the $\mu(I)$ rheology model has a friction coefficient μ, which is a function of the inertial number (Gray and Edwards 2014). For saturated soil, the dilatancy angle is a function of the solid volume fraction, and a linear formula is proposed to evaluate the dilatancy angle (Bouchut et al. 2016; Iverson and George 2014, 2016):

$$\tan\psi = \xi(m_s - m_{eq}), \tag{24}$$

where ψ is the dilatancy angle, m_{eq} is an equilibrium solid volume fraction, ξ is a calibration constant, and generally, $\xi = 1$ (Iverson and George 2014, 2016). Iverson and George (2014), uses a generalized dimensionless parameter N that allows $\sigma_e = 0$ to gauge the combined effects of the effective stress and shear strain-rate $\dot{\gamma} = \sqrt{\frac{1}{2}\dot{e}_{ij} \cdot \dot{e}_{ij}}$ on m_{eq} in the following form:

$$N = \frac{\mu\dot{\gamma}}{\rho_s \dot{\gamma}^2 \zeta^2 + \sigma_e}, \tag{25}$$

where μ is the effective shear viscosity of the pore fluid, $\dot{e}_{ij}$ is the deviatoric strain-rate tensor, and ζ is a characteristic grain diameter. Because our model allows $\sigma_e = 0$, the upper bound of N is limited in our model, considering that the perfect damping is physically irrelevant. According to Iverson and George (2014), the practical full-scale range of N is $0 \le N \le 1$. Iverson and George (2014) proposed a function of $m_{eq}(N)$:

$$m_{eq} = \frac{m_{crit}}{1 + \sqrt{N}}, \tag{26}$$

where m_{crit} is the critical state solid volume fraction of normally consolidated soils in the lithostatic stress state.

Stress–strain relationship

The undrained behavior of the saturated soil depends on both the void ratio after the consolidation and the effective confining stress (Konrad 1990). The minimum undrained strength is not unique, and it depends on the stress conditions (Konrad 1993). The minimum undrained strength is a crucial factor in judging whether or not the flow failure occurs (Ishihara et al. 1989; Uzuoka et al. 1998). The judgment standards of flow failure are formulated as

(a) $\tau_s \le \tau_{min}$: flow failure does not occur
(b) $\tau_s > \tau_{min}$: flow failure occurs,

where τ_s is the shear stress, and τ_{min} is the minimum shear strength. Our model applies the Drucker–Prager criterion to judge whether or not the flow failure occurs.

During the elastic stage, the stress increment-strain increment relationship of the soil can be calculated by

$$\Delta\sigma_{ij} = K_t\delta_{ij}\Delta\varepsilon_{kk} + 2G\Delta e_{ij}, \tag{27}$$

$$\sigma_{ij}^N = \sigma_{ij} + \Delta\sigma_{ij}, \tag{28}$$

$$\sigma_t^N = \frac{1}{3}\sigma_{kk}^N, \tag{29}$$

$$\Delta u_f = K_m\delta_{ij}\Delta\varepsilon_{kk}, \tag{30}$$

$$u_f^N = u_f + \Delta u_f + \Delta u_f^e, \tag{31}$$

where e_{ij} is the deviatoric strain tensor, G is the shear modulus, σ_{ij}^N is the new total stress tensor, σ_t^N is the new total mean stress, Δu_f^e is the excess pore fluid pressure increment, and u_f^N is the new pore fluid pressure. The volume strain increment $\Delta\varepsilon_v^e$ caused by the shear strain increment $\Delta\gamma$ can be evaluated as $\Delta\varepsilon_v^e = \Delta\gamma\tan\psi$; thus, the excess pore fluid pressure can be calculated by

$$\Delta u_{\mathrm{f}}^{\mathrm{e}} = K_{\mathrm{f}} \Delta\gamma \tan\psi. \tag{32}$$

The new effective stress $\sigma_{\mathrm{e}}^{\mathrm{N}}$ and the new second deviatoric shear stress τ^{N} are calculated using the formulae seen below.

$$\sigma_{\mathrm{e}}^{\mathrm{N}} = \frac{1}{3}\sigma_{kk}^{\mathrm{N}} - u_{\mathrm{f}}^{\mathrm{N}}, \tag{33}$$

$$s_{ij}^{\mathrm{N}} = \sigma_{ij}^{\mathrm{N}} - \sigma_{\mathrm{t}}^{\mathrm{N}}, \tag{34}$$

$$\tau^{\mathrm{N}} = \sqrt{\frac{1}{2} s_{\mathrm{ij}}^{\mathrm{N}} s_{ij}^{\mathrm{N}}}, \tag{35}$$

where s_{ij}^{N} is the new second invariant of the deviatoric stress tensor. Thus, the criterion is expressed as

$$f(\sigma_{\mathrm{e}}^{\mathrm{N}}, \tau^{\mathrm{N}}) = \sigma_{\mathrm{e}}^{\mathrm{N}} \tan(\phi + \psi) + \tau^{\mathrm{N}} - c, \tag{36}$$

where ϕ is the internal friction angle, and c is the cohesion.

Although the tensile strength of the saturated soil, effective stress, and pore fluid pressure cannot be positive, cohesion can exist. After inserting Eqs. (33) and (35) into (36), we need to conduct stress-state corrections (Chen and Mizuno 1990). The stress state can be corrected in two steps:

1. Corrections of the total mean stress and pore fluid pressure:

The corrected values of the total mean stress $\sigma_{\mathrm{t}}^{\mathrm{C}}$ and pore fluid pressure $u_{\mathrm{t}}^{\mathrm{C}}$ can be calculated by $\sigma_{\mathrm{t}}^{\mathrm{C}} = \max(\sigma_{\mathrm{t}}^{\mathrm{N}}, 0)$ and $u_{\mathrm{f}}^{\mathrm{C}} = \max(u_{\mathrm{f}}^{\mathrm{C}}, 0)$ respectively, where

$$\sigma_{\mathrm{t}} = \sigma_{\mathrm{t}}^{\mathrm{N}} - \sigma_{\mathrm{t}}^{\mathrm{C}}, \tag{37}$$

$$u_{\mathrm{f}} = u_{\mathrm{f}}^{\mathrm{N}} - u_{\mathrm{f}}^{\mathrm{C}}. \tag{38}$$

The pore fluid pressure cannot be less than the total mean stress. If $\sigma_{\mathrm{t}} > u_{\mathrm{f}}^{\mathrm{N}}$, $u_{\mathrm{f}} = u_{\mathrm{f}}^{\mathrm{N}} = \sigma_{\mathrm{t}}$, and $\sigma_{\mathrm{e}} = \sigma_{\mathrm{e}}^{\mathrm{N}} = \sigma_{\mathrm{t}} - u_{\mathrm{f}}$.

2. Shear stress corrections:

   (a) If $f(\sigma_{\mathrm{e}}^{\mathrm{N}}, \tau^{\mathrm{N}}) \le 0$, the corrections are not needed, and $\sigma_{ij} = s_{ij}^{\mathrm{N}} + \sigma_{\mathrm{t}}\delta_{ij}$.

   (b) If $f(\sigma_{\mathrm{e}}^{\mathrm{N}}, \tau^{\mathrm{N}}) > 0$, the corrections are essential, $\tau^{\mathrm{N}} = c - \tan(\psi + \phi)\sigma_{\mathrm{e}}^{\mathrm{N}}$, and the stress tensor is

$$\sigma_{ij} = \sigma_{\mathrm{t}}\delta_{ij} + \frac{\dot{e}_{ij}}{\dot{\gamma}}\tau^{\mathrm{N}} + 2(1 - m_{\mathrm{s}})\mu\dot{e}_{ij}. \tag{39}$$

Modeling the dynamics process of the Shenzhen landslide

Physical and mechanical parameters of the proposed model

The common physical and mechanical parameters, such as density, solid volume fraction, saturability, internal friction angle, modulus of compressibility, and cohesion have been tested by Ouyang et al. (2016) and Yin et al. (2016). The compression modulus of the samples was taken from the landslide surface and ranged between 2.5 and 4.5 MPa. In our simulation, the reference normal stress σ_0 is −4.5 MPa and the bulk modulus of water K_{w} is 2.15 GPa. The bulk modulus of the solid grains K_{s} is difficult to test, and the compression volume of the solid is far less than the compression volume of water; thus, in our simulation, K_{s} is chosen as 215 GPa to limit the maximum bulk modulus of the mixture. According to Iverson and George (2014, 2016), the recommended value for m_{crit} is 0.64. The characteristic grain diameter ζ is 0.01 m, the effective shear viscosity of the pore fluid μ is 0.001 N s/m^2, the proportionality coefficient b is 0.4, the cohesion c is 12 kPa, the shear modulus G is 6 MPa, the soil particle density ρ_{s} is 2650 kg/m^3, the internal friction angle ϕ is 30°, and the standard atmospheric pressure p_0^{a} is -0.1 MPa. The friction angle between the soil and the ground depends on frictional velocity weakening; the maximum basal friction angle is 30°, and the minimum basal friction angle is 25°. All the parameter values used in the numerical simulation are shown in Table 1.

Numerical results

Numerical results when $m_0 = 0.57$

The samples are unsaturated soils, and the void is filled by the water–air mixture. In our simulation, the soil in the source area is saturated, and according to Yin et al. (2016), an initial solid volume fraction m_0 of 0.57 is appropriate. The simulation results of the landslide flow velocity and dilatancy angles at different times are shown in Figs. 4 and 5, and the source area material migration displacement is shown in Fig. 6. Because the constructions are ignored, the range of the numerical deposition area on the right-hand side is larger than the range of the actual deposition area on the same side.

As shown in Fig. 4, the landfill collapses quickly within the first 50 s, and the maximum flow velocity can exceed 24 m/s. The direction of the landslide flow changes towards the left as the soil accumulates along the front edge of the initial flow direction. At $t = 200$ s, the maximum flow velocity at the edge of the deposition area decreases to below 2 m/s, and the expansion of the deposition area almost ceases. The maximum speed occurs at the north gap of the pit, where the steepest terrain is located.

As shown in Fig. 5a, b, the maximum source area material migration distance L_{M} is more than 960 m. The maximum vertical distance H_{M} is about 120 m, and thus, the equivalent friction angle, which is based on the ratio

Table 1 Parameter values used in the numerical simulations

Material property	Actual parameters in the simulation	Alternative parameters in the simulation
Initial solid volume fraction, m_0	0.57	0.57–0.64
Reference normal stress, σ_0 (MPa)	−4.5	−4.5
Bulk modulus of water, K_w (GPa)	2.15	2.15
Bulk modulus of solid particle, K_s (GPa)	215	215
Lithostatic critical-state solid volume, m_{crit}	0.64	0.64
Characteristic grain diameter, ζ (m)	0.01	0.01
Effective shear viscosity of pore fluid, μ (N s/m^2)	0.001	0.001
Proportionality coefficient, b	0.4	0.4
Cohesion, c (KPa)	12	12
Shear modulus of soil, G (MPa)	6	6
Soil particle density, ρ_s (kg/m^3)	2650	2650
Internal friction angle, ϕ (°)	30	30
Standard atmospheric pressure, p_0^a (MPa)	−0.1	−0.1

L_M/H_M (Legros 2002), is less than 7.2°. The friction angle between the landslide bottom and the ground is greater than 25°, and the internal friction angle is 30°. We can infer that the dilatancy angle and excess pore pressure during the landslide dynamic process conspicuously influence the runout process. As shown in Fig. 5c, when the Shenzhen landslide is simulated without considering the dilatancy angle, the runout distance is much less than the distance as represented in Fig. 5b. As shown in Fig. 5d, the maximum total displacement without the excess pore fluid pressure (the excess pore pressure is set to 0 Pa) is 820.4 m; thus, the equivalent friction angle is greater than 8°. The same figure shows that the range of the deposition area, simulated by the model without the excess pore fluid pressure or dilatancy angle, is much smaller than the range of the deposition area simulated by the dilatancy model.

As shown in Fig. 6, the minimum dilatancy angle tangent during the flow process is greater than −0.3287, which means that the dilatancy angle is greater than −18.2°. Comparing with Fig. 4, we find that the landslide flow velocity at the bottom is less than that at the surface, and the dilatancy angle at the bottom of the landslide deposit area is less than that at the surface of the landslide deposit area and source area. Therefore, the internal friction angle during the landslide flow process is greater than 11.8°, which exceeds the equivalent friction angle of the simulation results shown in Fig. 5b, d. This indicates that the excess pore fluid pressure caused by the dilatancy angle is an important factor for the landslide dynamic process.

Numerical results when m_0 is different

The dilatancy angle is an important factor affecting the dynamic process of a landslide. The dilatancy angle is related to the critical-state solid volume fraction m_{crit}, the generalized dimensionless parameter N, and the solid volume fraction m_s, which is controlled by the dilation and contraction of the mixture. Thus, we simulate the deposition range of the Shenzhen landslide at different initial solid volume fractions. The numerical results are shown in Fig. 7.

As shown in Fig. 7, the range of the deposition area increases with the decrease in the initial solid volume fraction angle. The landslide deposition area is conspicuous, when the initial solid fraction alters from 0.62 to 0.64. In contrast, the landslide deposition area changes slightly when the initial solid fraction alters from 0.57 to 0.62. The dilatancy angle is related to the difference between the current solid volume fraction m_s and the equilibrium solid volume fraction m_{eq}. The equilibrium solid volume fraction is less than the lithostatic critical-state solid volume fraction m_{crit}, which is equal to 0.64. This indicates that a little difference between m_0 and m_{crit} when $m_0 < m_{crit}$ can cause a huge expansion in the deposition area. The maximum displacement and the maximum kinetic energy are shown in Fig. 8.

As shown in Fig. 8, the maximum displacement of the landslide, L_M, decreases slowly when m_0 ranges between 0.57 and 0.63, and L_M decreases quickly when m_0 increases from 0.63 to 0.64. The maximum displacement decreases by 25 m as the initial solid volume fraction m_0 increases by 0.01 in the interval [0.57, 0.63], and the maximum displacement decreases by 695.8 m when m_0 increases from 0.63 to 0.64. The increment in L_M when m_0 decreases from 0.64 to 0.63 is nearly 28 times as much as the average increment in L_M with every 0.01 reduction in m_0 in the interval [0.63, 0.57].

The relationship between the kinetic energy and time at different initial solid volume fractions is shown in Fig. 9. The maximum kinetic energy decreases as the initial solid

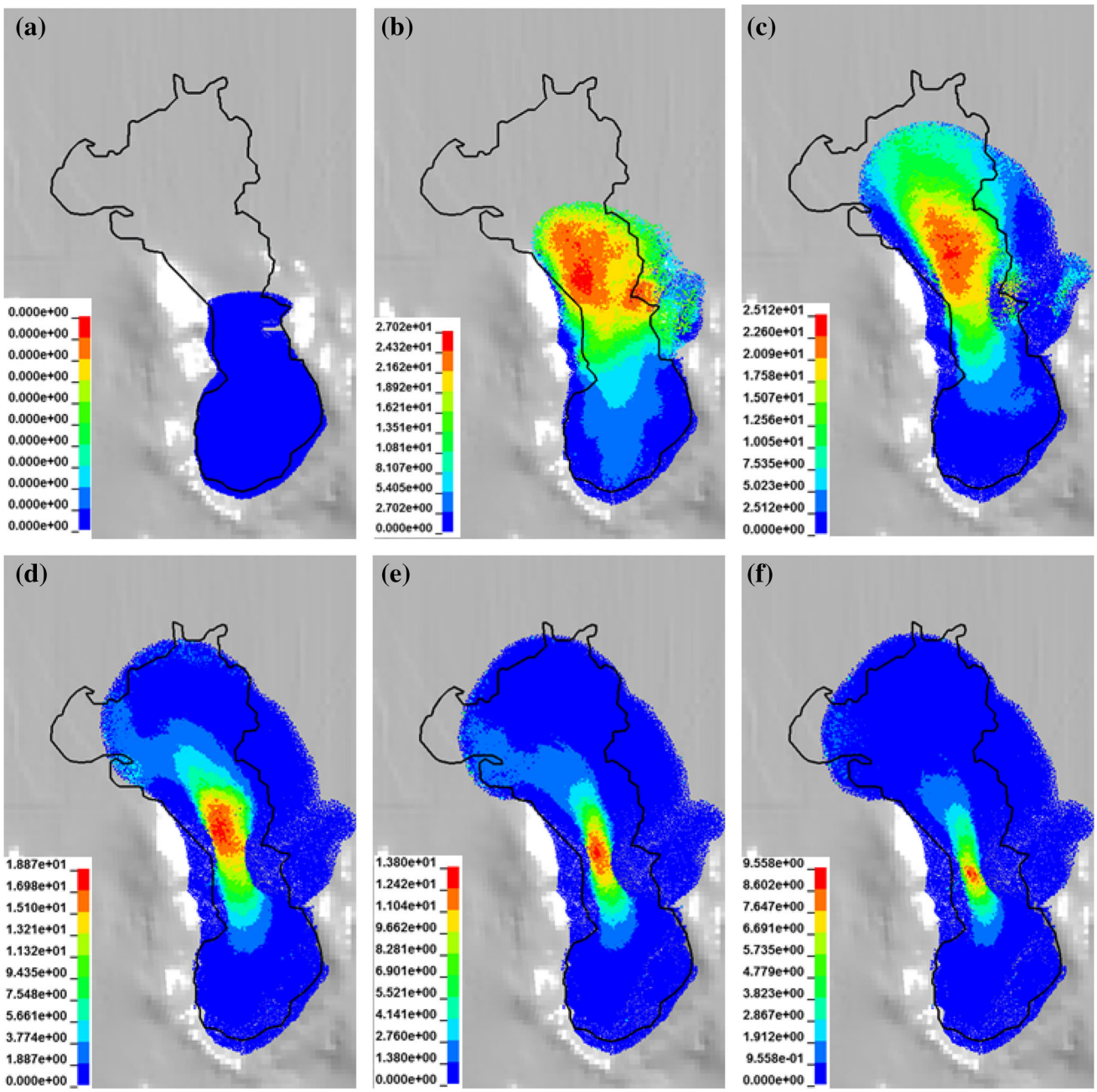

Fig. 4 The flow velocity (m/s) of the Shenzhen landslide. **a** $t = 0$ s; **b**, $t = 25$ s; **c** $t = 50$ s; **d** $t = 100$ s; **e** $t = 150$ s; **f** $t = 200$ s

volume fraction increases. When the initial solid volume fraction is 0.64, the maximum kinetic energy is 5.05×10^9 J, whereas when it is 0.57, the maximum kinetic energy is 3.18×10^{11} J. The maximum kinetic energy of the landslide when m_0 is 0.64 is about one-tenth of that when m_0 is 0.63. The average increment in the maximum kinetic energy when the initial solid volume fraction decreases by 0.01 in the interval of [0.57, 0.64] is 4.47×10^{10} J, which is nearly nine times as much as the maximum kinetic energy when the initial solid volume fraction is equal to 0.64.

Conclusion

In this paper, we propose a dilatancy constitutive model simulating the flow behavior of the landslide assuming there is no water supplement during the flow process. In this model, the consolidation and matric suction are ignored, the fluid phase and soil particles are compressible, and air is insoluble. This model couples the excess pore fluid pressure with the evolving dilatancy angle, which plays an important role in simulating the flow behavior of the landslide containing saturated geomaterials. The

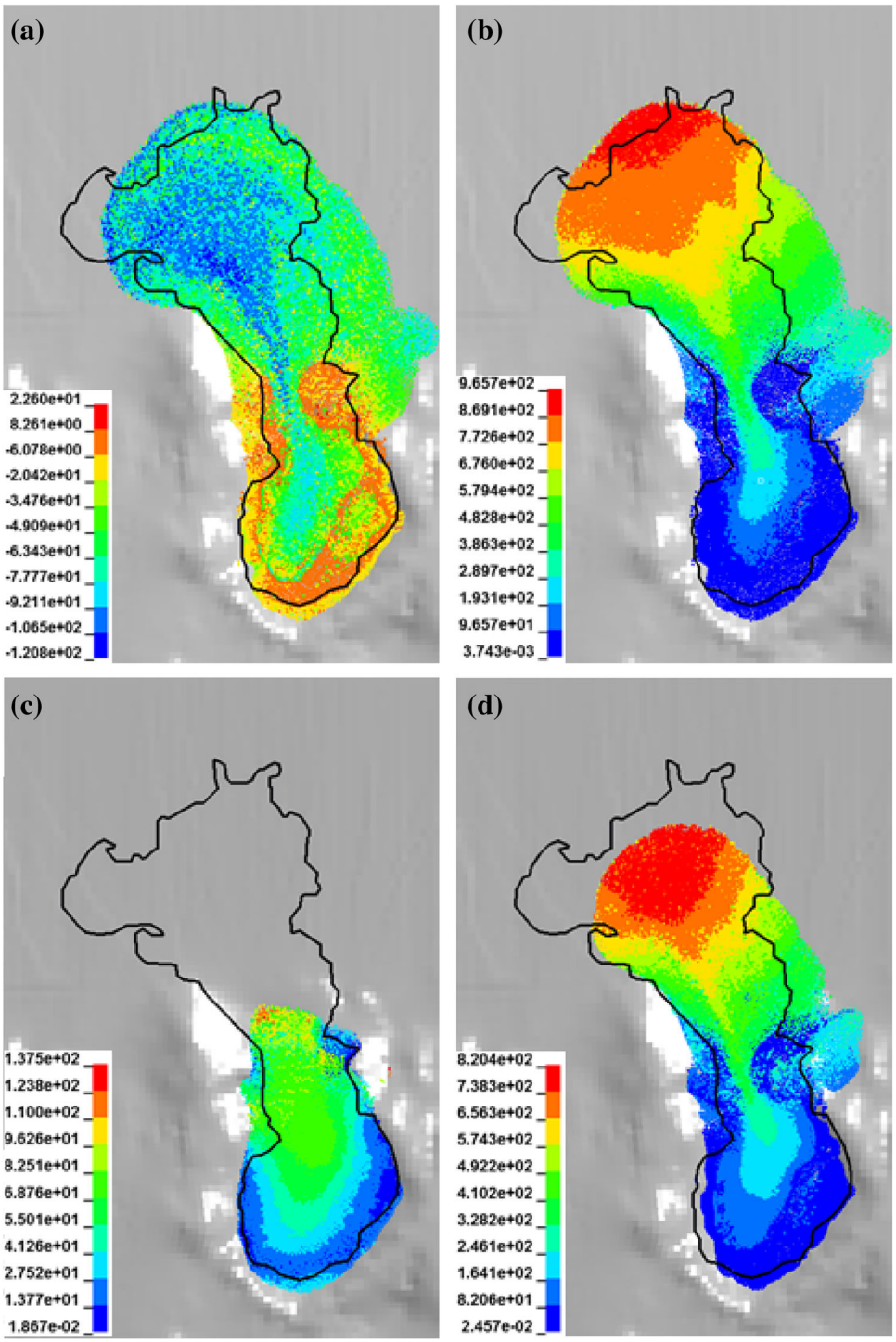

Fig. 5 The movement distance (m) of the Shenzhen landslide ($t = 200$ s). **a** The vertical distance; **b** the total distance; **c** the total distance without shear dilation; and **d** the total distance without excess pore fluid pressure

dilatancy angle ψ is related to the current solid volume fraction m_s and the equilibrium solid volume fraction m_{eq}; the excess pore fluid pressure is related to the dilatancy angle ψ and the shear strain. This model is suitable for studying landslides in which consolidation can be ignored during the flow process.

The model is applied to simulate an abrupt landslide that occurred at the Hong'ao Village CSW landfill in Shenzhen, China. The numerical results show that our model can simulate the flow process of the Shenzhen landslide. The shape and range of the landslide deposition area obtained by the simulation are consistent with the shape and range of the actual landslide deposition. The dilatancy angle and the excess pore fluid pressure play an important role in the Shenzhen landslide flow process.

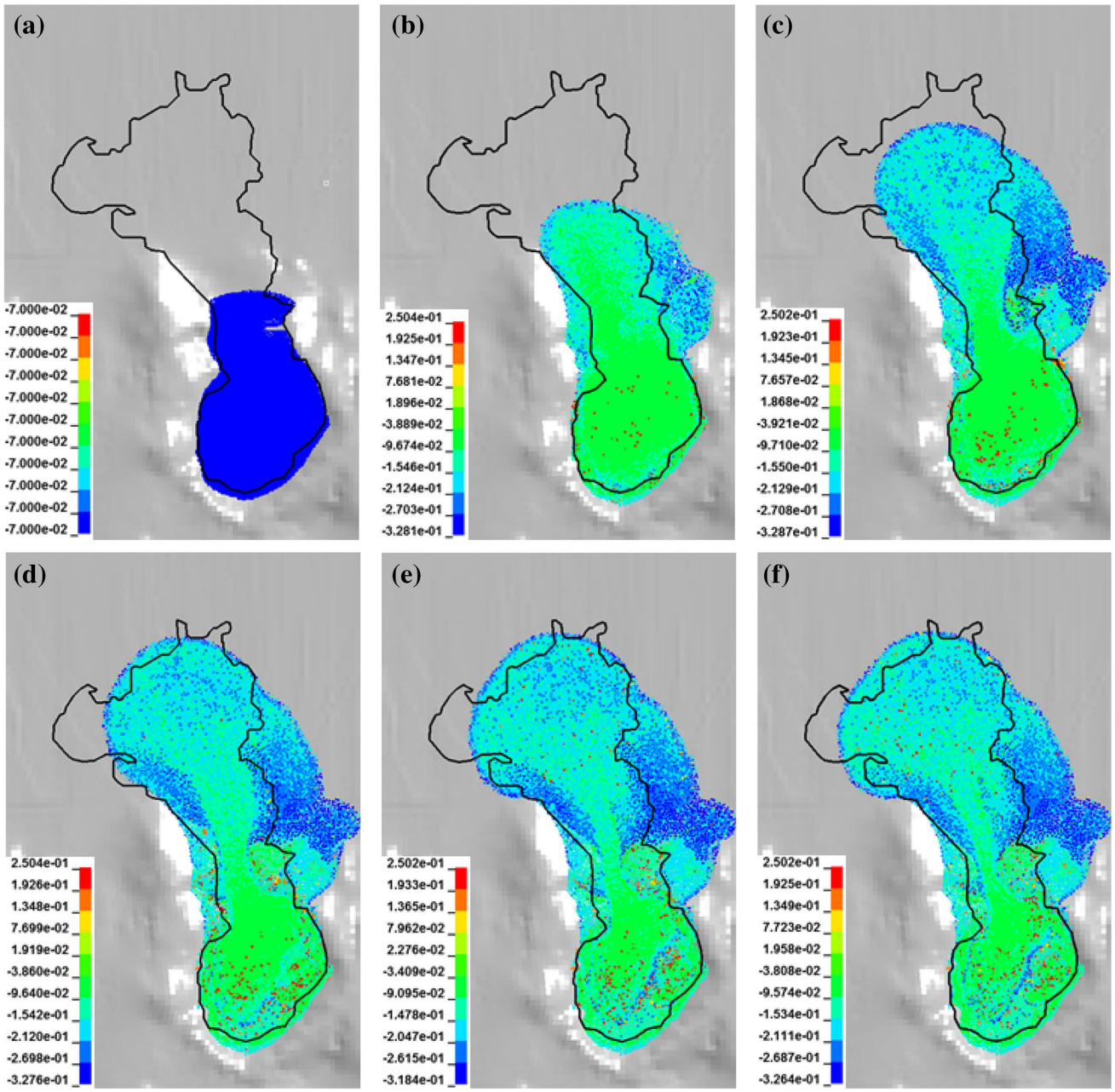

Fig. 6 The tangent of the dilatancy angle at the Shenzhen landslide

The deposition form, the source area material migration displacement L, and kinetic energy of the Shenzhen landslide are simulated at different initial solid volume fractions. The maximum displacement of the source area material migration L_M is related to the initial solid volume fraction m_0. The increment in L_M, when m_0 is decreased from 0.64 to 0.63, is nearly 28 times as much as the average increment value in L_M with every 0.01 reduction of m_0 in the interval [0.63, 0.57]. The maximum kinetic energy of the landslide when $m_0 = 0.64$ is about one-tenth of that when $m_0 = 0.63$, and the maximum kinetic energy increment with every 0.01 reduction in m_0 in the interval [0.64, 0.57] is about nine times as much as the maximum kinetic energy of the landslide when m_0 is 0.64.

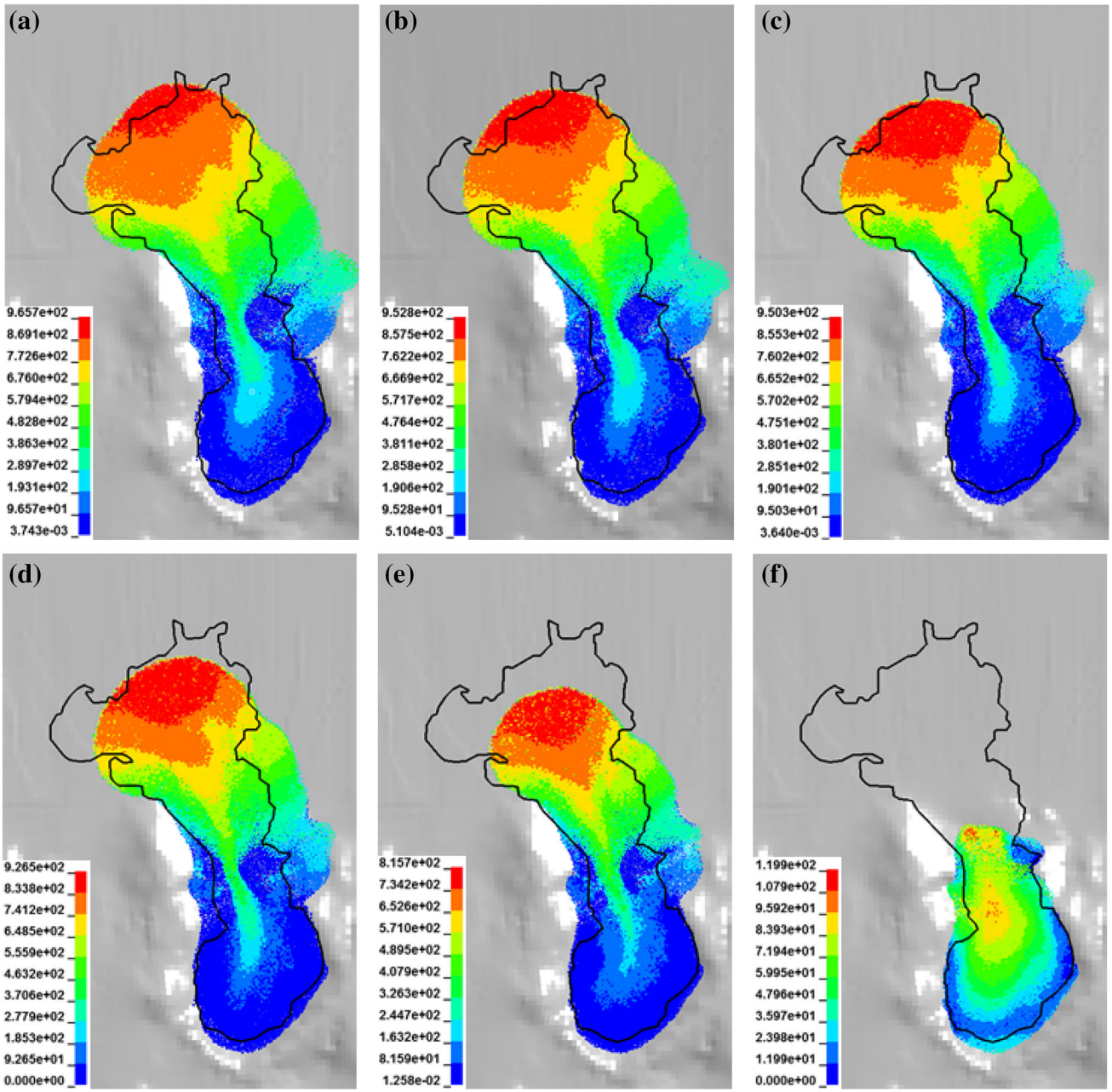

Fig. 7 The deposition area and displacements of different solid volume fractions at $t = 200$ s. **a** $m_0 = 0.57$; **b** $m_0 = 0.59$; **c** $m_0 = 0.61$; **d** $m_0 = 0.62$; **e** $m_0 = 0.63$; and **f** $m_0 = 0.64$

The numerical modeling results of the Shenzhen landslide indicate that the dilatancy model is suitable to simulate the flow process of saturated and low-hydraulic permeability landslides. If $m_0 < m_{crit}$ before the landslide occurs, the shear strain causes shear contraction behavior, the pore fluid pressure increases, and the effective stress decreases. Then, soil liquefaction and landslide flow motion occur. If $m_0 > m_{crit}$ exists before the landslide takes place, the shear strain causes dilatancy behavior, the pore fluid pressure decreases, and the effective stress increases. This may lead the source area to become more stable and reduce landslide risks. The dilatancy model and numerical

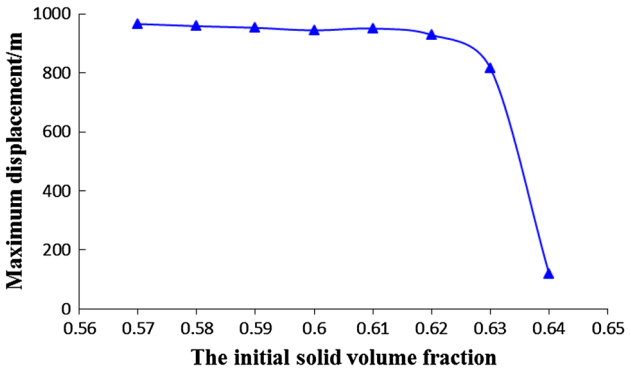

Fig. 8 The maximum displacement-initial solid volume fraction curve at $t = 200$ s

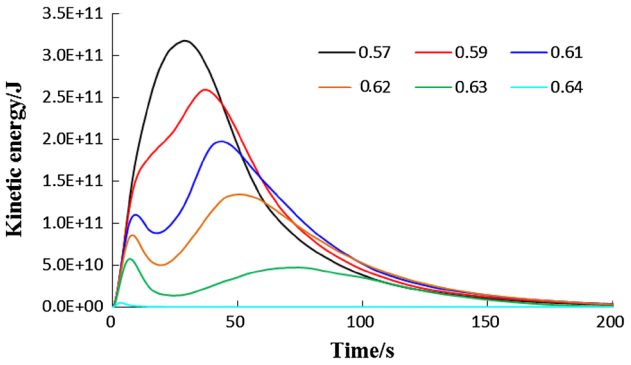

Fig. 9 The kinetic energy-time curve

results also indicate that proper measures, such as compaction and drainage, may effectively increase the stability of such slopes.

Acknowledgments This work was supported as a joint research project by NSFC-ICIMOD (Grant no. 41661144041) and the Science and Technology Department of Sichuan Province of China (Grant no. 2016SZ0067).

References

Anderson JD, Wendt J (1995) Computational fluid dynamics, vol 206. McGraw-Hill, New York

Bolton MD (1984) The strength and dilatancy of sands. Cambridge University Engineering Department

Bouchut F, Fernández-Nieto ED, Mangeney A, Narbona-Reina G (2016) A two-phase two-layer model for fluidized granular flows with dilatancy effects. J Fluid Mech 801:166–221

Cascini L, Cuomo S, Pastor M, Sorbino G, Piciullo L (2012) Modeling of propagation and entrainment phenomena for landslides of the flow type: the May 1998 case study. In: Landslides and engineered slopes: protecting society through improved understanding. Proceedings of the 11th International and 2nd North American Symposium on Landslides, vol 38, pp 1723–1729, Chirico

Cascini L, Cuomo S, Pastor M, Sorbino G, Piciullo L (2014) SPH run-out modelling of channelised landslides of the flow type. Geomorphology 214:502–513

Chen CL (1987) Comprehensive review of debris flow modeling concepts in Japan. Rev Eng Geol 7:13–30

Chen WF, Mizuno E (1990) Nonlinear analysis in soil mechanics. Elsevier, Amsterdam, pp 143–150

Cola S, Calabrò N, Pastor M (2008) Prediction of the flow-like movements of Tessina landslide by SPH model. Landslides and engineered slopes. Taylor & Francis Group, London

Colomer-Mendoza FJ, Esteban-Altabella J, García-Darás F, Gallardo-Izquierdo A (2013) Influence of the design on slope stability in solid waste landfills. Earth Sci 2(2):31–39

Davies TR, McSaveney MJ (2009) The role of rock fragmentation in the motion of large landslides. Eng Geol 109(1):67–79

Fung YC, Tong P (2001) Classical and computational solid mechanics, vol 1. World Scientific

George DL, Iverson RM (2014) A depth-averaged debris-flow model that includes the effects of evolving dilatancy: II. Numerical predictions and experimental tests. Proc R Soc A 470(2170):20130820

Gray JMNT, Edwards AN (2014) A depth-averaged-rheology for shallow granular free-surface flows. J Fluid Mech 755:503–534

Haddad B, Pastor M, Palacios D, Munoz-Salinas E (2010) A SPH depth integrated model for Popocatépetl 2001 lahar (Mexico): sensitivity analysis and runout simulation. Eng Geol 114:312–329

Huang Y, Dai Z (2014) Large deformation and failure simulations for geo-disasters using smoothed particle hydrodynamics method. Eng Geol 168:86–97

Huang Y, Zhang W, Mao W, Jin C (2011) Flow analysis of liquefied soils based on smoothed particle hydrodynamics. Nat Hazards 59:1547–1560

Huang Y, Zhang W, Xu Q, Xie P, Hao L (2012) Run-out analysis of flow-like landslides triggered by the Ms 8.0 2008 Wenchuan earthquake using smoothed particle hydrodynamics. Landslides 9:275–283

Huang Y, Dai Z, Zhang W, Huang M (2013) SPH-based numerical simulations of flow slides in municipal solid waste landfills. Waste Manage Res 31:256–264

Hutter K, Laloui L, Vulliet L (1999) Thermodynamically based mixture models of saturated and unsaturated soils. Mech Cohes Frict Maters 4:295–338

Ishihara K, Yasuda S, Yoshida Y (1989) Liquefaction-induced flow failure of embankments and residual strength of silty sands. Sino-Japan Joint Symposium on Improvement of Weak Ground, pp 69–80

Iverson RM (2000) Landslide triggering by rain infiltration. Water Resour Res 36:1897–1910

Iverson RM (2003) The debris-flow rheology myth[C]. Debris Flow Hazards Mitig Mech Predict Assess 1:303–314

Iverson RM (2005) Regulation of landslide motion by dilatancy and pore pressure feedback. J Geophys Res Earth Surf 110(F2):273–280

Iverson RM, George DL (2014) A depth-averaged debris-flow model that includes the effects of evolving dilatancy. I. Physical basis. Proc R Soc A 470(2170):20130819

Iverson RM, George DL (2016) Modelling landslide liquefaction, mobility bifurcation and the dynamics of the 2014 Oso disaster. Géotechnique 66:175–187

Iverson RM, Reid ME, Iverson NR, LaHusen RG, Logan M, Mann JE, Brien DL (2000) Acute sensitivity of landslide rates to initial soil porosity. Science 290:513–516

Jackson R (2000) The dynamics of fluidized particles. Cambridge University Press

Konrad JM (1990) Minimum undrained strength of two sands. J Geotech Eng 116:932–947

Konrad JM (1993) Undrained response of loosely compacted sands during monotonic and cyclic compression tests. Géotechnique 43:69–89

Legros F (2002) The mobility of long-runout landslides. Eng Geol 63:301–331

Liu GR, Gu YT (2005) An introduction to meshfree methods and their programming. Springer, Berlin

Liu GR, Liu MB (2003) Smoothed particle hydrodynamics: a meshfree particle method. World Scientific

Liu MB, Liu GR (2010) Smoothed particle hydrodynamics (SPH): an overview and recent developments. Arch Comput Methods Eng 17:25–76

Lucas A, Mangeney A, Ampuero JP (2014) Frictional velocity-weakening in landslides on Earth and on other planetary bodies. Nat Commun 5:3417

Lucy LB (1977) A numerical approach to the testing of the fission hypothesis. Astronom J 82:1013–1024

Major JJ (2000) Gravity-driven consolidation of granular slurries: implications for debris-flow deposition and deposit characteristics. J Sediment Res 70:64–83

Major JJ, Iverson RM, McTigue DF, Macias S, Fiedorowicz BK (1997) Geotechnical properties of debris-flow sediments and slurries. In: Proceedings of the 1997 1st International Conference on Debris-Flow Hazards Mitigation: Mechanics, Prediction, and Assessment, pp 249–259

McDougall S, Hungr O (2005) Dynamic modelling of entrainment in rapid landslides. Can Geotech J 42:1437–1448

Ochiai H, Okada Y, Furuya G, Okura Y, Matsui T, Sammori T, Terajima T, Sassa K (2004) A fluidized landslide on a natural slope by artificial rainfall. Landslides 1:211–219

Ouyang C, Zhou K, Xu Q, Yin J, Peng D, Wang D, Li W (2016) Dynamic analysis and numerical modeling of the 2015 catastrophic landslide of the construction waste landfill at Guangming, Shenzhen, China. Landslides 1–14

Pailha M, Pouliquen O (2009) A two-phase flow description of the initiation of underwater granular avalanches. J Fluid Mech 633:115–135

Pastor M, Blanc T, Pastor MJ (2009a) A depth-integrated viscoplastic model for dilatant saturated cohesive-frictional fluidized mixtures: application to fast catastrophic landslides. J Nonnewton Fluid Mech 158:142–153

Pastor M, Haddad B, Sorbino G, Cuomo S, Drempetic V (2009b) A depth-integrated, coupled SPH model for flow-like landslides and related phenomena. Int J Num Anal Meth Geomech 33:143–172

Pastor M, Blanc T, Haddad B, Petrone S, Morles MS, Drempetic V, Issler D, Crosta GB, Cascini L, Sorbino G, Cuomo S (2014) Application of a SPH depth-integrated model to landslide run-out analysis. Landslides 11:793–812

Sheng D, Fredlund DG, Gens A (2008) A new modelling approach for unsaturated soils using independent stress variables. Can Geotech J 45:511–534

Sheng LT, Tai YC, Kuo CY, Hsiau SS (2013) A two-phase model for dry density-varying granular flows. Adv Powder Technol 24:132–142

Uzuoka R, Yashima A, Kawakami T, Konrad JM (1998) Fluid dynamics based prediction of liquefaction induced lateral spreading. Comput Geotech 22:243–282

Violeau D (2012) Fluid mechanics and the SPH method: theory and applications. Oxford University Press, Oxford

Wang G, Sassa K (2003) Pore-pressure generation and movement of rainfall-induced landslides: effects of grain size and fine-particle content. Eng Geol 69:109–125

Yin Y, Li B, Wang W, Zhan L, Xue Q, Gao Y, Zhang N, Chen H, Liu T, Li A (2016) Mechanism of the December 2015 catastrophic landslide at the Shenzhen landfill and controlling geotechnical risks of urbanization. Engineering 2:230–249